View metadata, citation and similar papers at core.ac.uk

brought to you by CORE

provided by Caltech Authors - Main

Check for updates

# Configurational entropy of basaltic melts in Earth's mantle

Sung Keun Lee[a,b,1], Jed L. Mosenfelder[c], Sun Young Park[a], A. Chim Lee[a], and Paul D. Asimow[d]

[a]School of Earth and Environmental Sciences, Seoul National University, 08826 Seoul, Korea; [b]Institute of Applied Physics, Seoul National University, 08826 Seoul, Korea; [c]Department of Earth Sciences, University of Minnesota, Minneapolis, MN 55415; and [d]Division of Geological & Planetary Sciences, California Institute of Technology, Pasadena, CA 91125

Edited by W. G. Ernst, Stanford University, Stanford, CA, and approved August 5, 2020 (received for review July 10, 2020)

**Although geophysical observations of mantle regions that suggest the presence of partial melt have often been interpreted in light of the properties of basaltic liquids erupted at the surface, the seismic and rheological consequences of partial melting in the upper mantle depend instead on the properties of interstitial basaltic melt at elevated pressure. In particular, basaltic melts and glasses display anomalous mechanical softening upon compression up to several GPa, suggesting that the relevant properties of melt are strongly pressure-dependent. A full understanding of such a softening requires study, under compression, of the atomic structure of primitive small-degree basaltic melts at their formation depth, which has proven to be difficult. Here we report multiNMR spectra for a simplified basaltic glass quenched at pressures up to 5 GPa (corresponding to depths down to ∼150 km). These data allow quantification of short-range structural parameters such as the populations of coordination numbers of Al and Si cations and the cation pairs bonded to oxygen atoms. In the model basaltic glass, the fraction of $^{[5,6]}$Al is ∼40% at 5 GPa and decreases to ∼3% at 1 atm. The estimated fraction of nonbridging oxygens at 5 GPa is ∼84% of that at ambient pressure. Together with data on variable glass compositions at 1 atm, these results allow us to quantify how such structural changes increase the configurational entropy of melts with increasing density. We explore how configurational entropy can be used to explain the anomalous mechanical softening of basaltic melts and glasses.**

configurational entropy | embryonic basaltic melts in Earth's mantle | anomalous compression of melts

Basalts erupted at midocean ridges (MOR) on the Earth's surface form oceanic crust and open a narrow window to look at the nature of the mantle (1). Their compositions offer a guide to the kinds of melts that might be present in the upper mantle at depths extending up to 150 km (∼5 GPa), especially in the presence of volatile components (2–6). The presence of a small fraction of such melts at the lithosphere–asthenosphere boundary (LAB) plays an important role in mantle flow and plate movement (e.g., refs. 7–11), and more broadly, the evolution of the silicate Earth and its reservoirs has been controlled by the separation of melts from their solid residues. The estimation of melt fraction from inversion of seismic data, the impact of such a melt fraction on the rheology of the asthenosphere, and the direction and rate of chemical segregation due to melting all depend on the thermomechanical and transport properties of silicate melts at high pressure, which are significantly different from those at 1 atm. For example, the viscosity of basaltic melts decreases with increasing pressure up to ∼5 GPa and then increases with further increase in pressure (10, 12). Basaltic glasses are also reported to undergo anomalous softening upon densification: unlike solids, whose wave speeds increase with compression in the absence of phase transitions, the compressional ($V_P$) and shear wave velocities ($V_S$) of basaltic melts and glasses show minima at ∼2 to 5 GPa, partly affecting the seismic properties of upper mantle (13–15). A mechanistic and predictive understanding of the phenomenon has proven elusive. The consequences of melt segregation in the Earth's interior also depend on the partitioning of trace elements between those melts and solid minerals. Because melts are structurally more flexible than crystalline analogs (16, 17), a wide range of metal cations preferentially partition into silicate melts. Experimental studies show that the partitioning of elements into silicate melts depends on pressure (18–24), often changing the order of compatibility, but in contrast to the fairly well-developed theories that explain the dependence of trace element partitioning on atomic-scale site parameters in solids (24), there is not presently a theory to predict the effect of changes in melt structure under compression on partitioning (e.g., refs. 22, 25, and 26 and *SI Appendix*, section S1).

Our ability to infer the presence of melts at depth in the mantle, to constrain their abundance from geophysical and geochemical observations, and to describe the influence of such melting on the evolution of the mantle depends on the differences between the melts that erupt on the surface and the melts that are present at depth. It is appreciated that melts evolve in composition from their deep sources as they ascend, mix with shallower melts, and react with rocks along their path. Inferences about melting at depth must consider exotic compositions that may never be sampled directly. It is less widely appreciated that the structural characteristics of melts and therefore their buoyancy and seismic signatures evolve with pressure as well. Hence, it is necessary to study the atomic structures of primary melts at pressures up to ∼5 GPa. While X-ray scattering is useful to distinguish the structures of silicate melts with simple compositions

## Significance

**Proper inference of the seismological and chemical effects of partial melting in Earth's upper mantle depends on physical properties of interstitial melts at elevated pressure. Silicate liquids display anomalous softening upon compression. This lacks an atomic-scale explanation, partly because studies linking microstructure and physical properties of melts are limited to ambient pressure. Here we studied basaltic glass quenched from high pressure with multinuclear NMR spectroscopy that defines the populations of oxygen species in the glass with sufficient precision to reveal a decrease with pressure in the configurational entropy, which we attribute to entanglement of the melt network upon densification. We explain how the configurational entropy can be used as a tool to explain the anomalous behavior of melts under compression.**

Author contributions: S.K.L. designed research; S.K.L., J.L.M., and S.Y.P. performed research; S.K.L., J.L.M., S.Y.P., and P.D.A. contributed new reagents/analytic tools; S.K.L., S.Y.P., and A.C.L. analyzed data; and S.K.L., J.L.M., and P.D.A. wrote the paper.

The authors declare no competing interest.

This article is a PNAS Direct Submission.

Published under the PNAS license.

[1]To whom correspondence may be addressed. Email: sungklee@snu.ac.kr.

This article contains supporting information online at https://www.pnas.org/lookup/suppl/doi:10.1073/pnas.2014519117/-/DCSupplemental.

First published August 24, 2020.



Downloaded at California Institute of Technology on September 8, 2020

at both 1 atm and high pressure, the application of X-ray scattering to multicomponent silicate glasses is challenging due to overlaps among binary correlation functions [e.g., (Si, Al)-O, (Mg, Fe)-O, and Ca-O] (*SI Appendix*, section S2). Advances in solid-state NMR, by contrast, provide unequivocal measurements of the atomic structures of complex silicate melts (e.g., cation coordination number and the populations of bridging oxygen [BO] atoms bonded to network formers [Si and Al] and of nonbridging oxygens [NBO] bonded to network modifiers [$Ca^{2+}$ and $Mg^{2+}$]; refs. 17 and 27) (*SI Appendix*, section S1). This opens a window to look at the structural evolution of multicomponent systems approaching the complexity of natural melts. Here we examine a popular model basalt composition (28, 29), the quaternary aluminosilicate melt near the eutectic between diopside [$CaMgSi_2O_6$ (Di)] and anorthite [$CaAl_2Si_2O_8$ (An)], ($Di_{64}An_{36}$) quenched from melts at high temperature (up to 2,100 K) and pressure up to 5 GPa, and a family of glasses in the system $SiO_2$-$TiO_2$-$Al_2O_3$-MgO-CaO-$Na_2O$-$K_2O$ that represents progressive changes with pressure in the composition of partial melts of peridotite (30, 31) (*SI Appendix*, section S3, and *Materials and Methods*). As the liquids are quenched into glasses, the structures of supercooled liquids at the glass transition temperature are explored (*SI Appendix*, section S4).

The mechanisms that accommodate densification of basaltic liquids up to a few GPa have been suggested to be largely topological (i.e., changes in bond angles and ring sizes; ref. 32) without changes in short-range structure (e.g., coordination number and degree of network polymerization) (33, 34). However, changes in the degree of melt polymerization upon compression have also been linked to changes in melt properties (13, 14, 35–37). Our NMR spectra plainly demonstrate noticeable changes in the short-range structure of $Di_{64}An_{36}$ glass within the first few GPa of compression. Fig. 1, *Top*, shows two-dimensional (2D) $^{27}Al$ NMR spectra, showing that four-coordinated Al ($^{[4]}Al$) is dominant (~97%) at 1 atm but decreases dramatically with pressure. At 3 GPa, the fractions of $^{[4]}Al$, $^{[5]}Al$, and $^{[6]}Al$ are ~75, ~16, and ~9%, respectively. At 5 GPa, those fractions are ~60, ~24, and ~16% (Fig. 1, *Bottom Right*, and *SI Appendix*, section S5 and Table S1). These changes reflect compression of a glass of constant composition. In equilibrium with mantle residues, however, the composition of basalt varies with depth, so it is important to constrain the effect of composition on the melt structure as well. In particular, the MgO content of basaltic glass increases with increasing formation pressure (30); this trend is represented by the three iron-free model basaltic glasses that we synthesized to approximate liquids in equilibrium with KLB-1 peridotite at 1, 1.5, and 3 GPa (*SI Appendix*, section S3). At 1 atm, the fractions of $^{[5,6]}Al$ in these glasses increase only slightly with increasing MgO content (Fig. 1, *Bottom Left*, and *SI Appendix*, Table S2) (31). Therefore, while the fractions of $^{[5,6]}Al$ in Mg-rich basaltic glasses at high pressure may be subtly different from those in the model basaltic glass, the trend in Al coordination environments with pressure at constant composition should be a reasonable approximation of the trend due to superimposed pressure and composition changes along the peridotite solidus (*SI Appendix*, section S3).



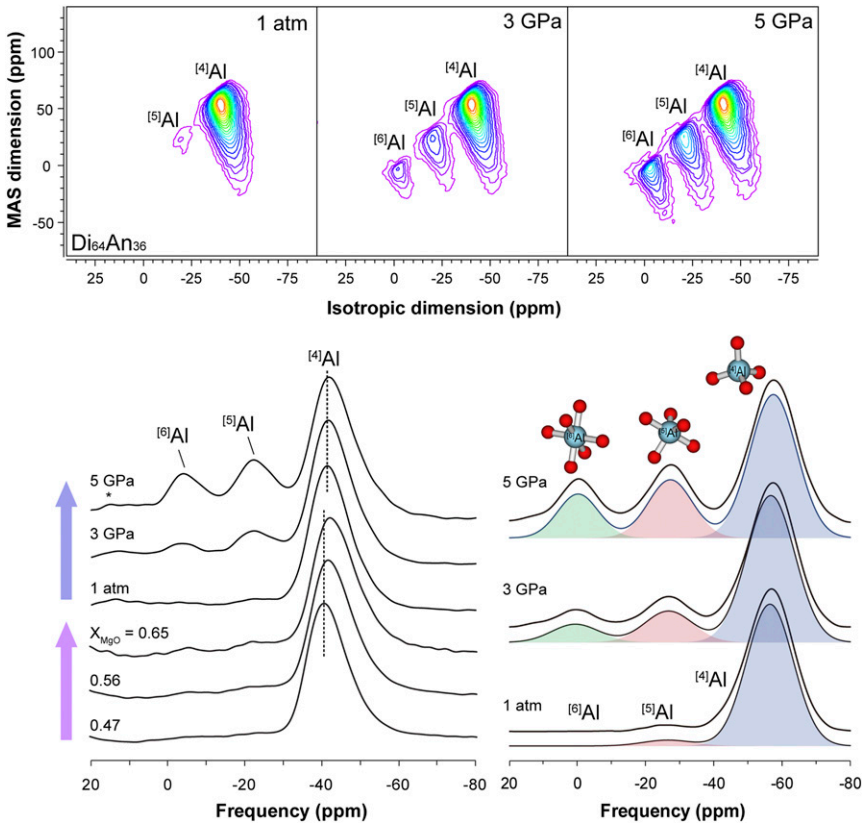


**Fig. 1.** Al environments in model basaltic glasses under compression up to 5 GPa. (*Top*) The $^{27}Al$ 3QMAS NMR spectra for the model basaltic glasses (CaO:MgO:$Al_2O_3$:$SiO_2$ = 25:16:9:50 mol %, CMAS) quenched from melts at 1 atm (1,673 K), 3 GPa (1,873 K), and 5 GPa (2,100 K) (*Materials and Methods*). Contour lines are drawn at 5% intervals from 3 to 98% of relative intensity. (*Bottom Left*) Total isotropic projection of $^{27}Al$ 3QMAS NMR spectra for the basaltic glasses quenched from melts at 1 atm, 3 GPa, and 5 GPa. The spectra for basaltic glasses with varying MgO concentration at 1 atm formed from melting of KLB-1 peridotite are also shown for comparison (see *SI Appendix*, Table S2, for the composition of the basaltic glasses with varying MgO content). (*Bottom Right*) Isotropic projection of the sheared 2D NMR spectra, which improves quantification of Al sites in multicomponent oxide glasses (*SI Appendix*, section S2 and Fig. S1).

Downloaded at California Institute of Technology on September 8, 2020

We extend our analysis of glass structure beyond the Al coordination numbers by collecting NMR spectra on oxygen nuclei: $^{17}$O NMR spectra for the glasses at 1 atm and 3 GPa indeed show BO, such as $^{[4]}$Si-O-$^{[4]}$Si, Si-O-$^{[4]}$Al, $^{[4]}$Si-O-$^{[5,6]}$Al, and $^{[4]}$Al-O-$^{[4]}$Al, and NBO including {Ca, Mg}-O-$^{[4]}$Si (Fig. 2, *Top*), although these peaks are not fully resolved. The Si-O-$^{[5,6]}$Si peak is not observed, as expected from the lack of a $^{[5,6]}$Si peak in the $^{29}$Si MAS NMR spectra of any of the studied glasses (*SI Appendix*, section S6 and Fig. S2). This result confirms that Al in basaltic glass is more likely than Si to be highly coordinated at pressures of 2 to 5 GPa (35, 37–39). The $^{17}$O NMR spectra reveal a decrease in Ca-NBO peak intensity with increasing pressure (Fig. 2, *Bottom Left*). The NBO fraction ($X_{NBO}$) is ~38% at 1 atm but decreases significantly with pressure to ~32% at 5 GPa (*SI Appendix*, section S7). Pressure-induced changes in the normalized $X_{NBO}$ are shown in Fig. 2, *Bottom Right*, together with previous measurement of NBO fractions in other silicate glasses (26, 40). While the normalized $X_{NBO}$ tends to decrease with increasing pressure in all these datasets, the model basaltic glasses studied here highlight the largest decrease thus far observed in $X_{NBO}$ with pressure among geologically relevant aluminosilicate melts. This decrease is due to the presence of high-field strength cations, such as Ca and Mg, and an intermediate degree of network polymerization at 1 atm (*SI Appendix*, section S1).

The current results confirm that the decrease in $X_{NBO}$ for basaltic melts from 1 atm to 5 GPa is accompanied by a dramatic increase in $^{[5,6]}$Al. Taking these changes into consideration, Fig. 3 depicts a mechanism for structural evolution of basaltic glasses upon compression where the increase in Al coordination number is facilitated by the formation of $^{[4]}$Si-O-$^{[5,6]}$Al BO at the expense of $^{[4]}$Si-O-{Ca,Mg} NBO. The resulting increase in connectivity of the network leads to the formation of smaller rings at the expense of larger rings by a ring-twisting mechanism. These coupled changes in short-range structure (coordination numbers) and medium-range structure (topology of the melt network) together accommodate densification. This structural evolution resembles the formation of multiple ring structures in a pretzel, as shown schematically in Fig. 3, *Bottom*. The knot in a pretzel corresponds to a $^{[4]}$Si-O-$^{[5,6]}$Al linkage. Such pressure-induced twists in the amorphous network are similar to lattice distortions in some crystalline lattices upon densification (e.g., $MgSiO_3$ bridgmanite) (41). Fig. 3, *Bottom*, is a schematic and simplified description of the structural transitions in the glasses under compression; the actual compression in multicomponent silicate melts can be more complex. The current model illustrates a possible configurational (and thus topological) change in the glasses upon compression. A reduction in ring size in oxide glasses has been linked to the formation of highly coordinated metal cations (42), similar to the earlier models based on solid-state NMR measurements (37, 39, 43). A topological evolution model showed that a straight pyroxene-like chain of tetrahedra, when shortened along the chain by kinking the Si-O-Si bond angles, reaches a critical shortening at which the atomic positions are identical to a chain of face-sharing octahedra (44). These models address the importance of topological contraction of the melt network. We extend these approaches to account for the

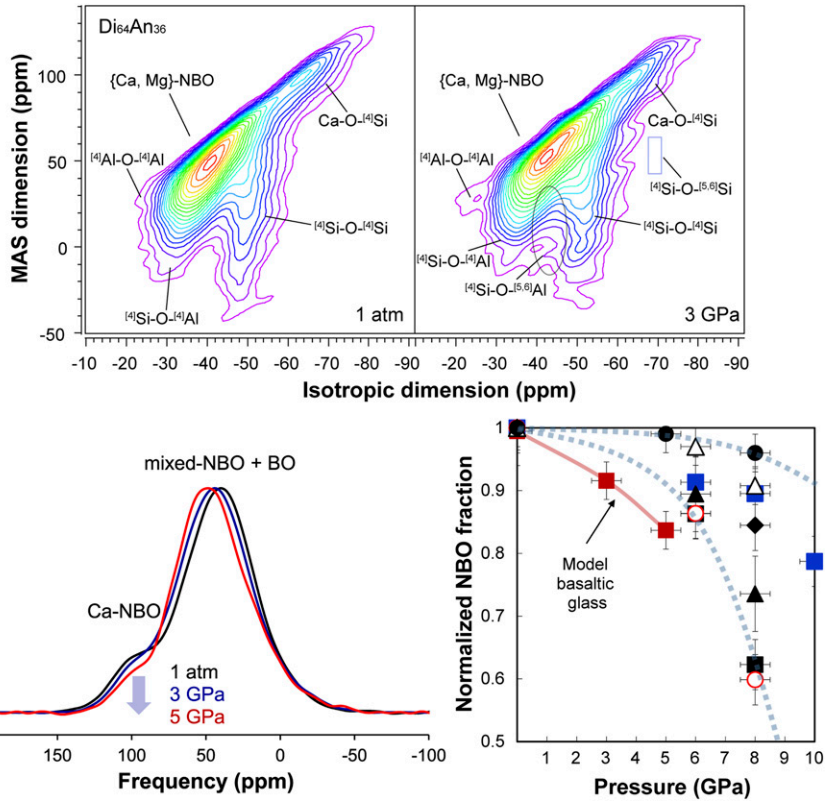


**Fig. 2.** O environments in model basaltic glasses under compression up to 5 GPa. (*Top*) The $^{17}$O 3QMAS NMR spectra for the model CMAS basaltic glasses quenched from melts at 1 atm and 3 GPa. (*Bottom Left*) The $^{17}$O MAS NMR spectra for the CMAS glasses quenched from melts at high pressure up to 5 GPa. (*Bottom Right*) Variation in the normalized NBO fraction in model basaltic glasses with pressure [$X_{NBO}$ for each composition is scaled to be 100% at 1 atm, $X_{NBO}$ ($P$)/$X_{NBO}$ (1 atm)] (red square). The normalized NBO fractions in other binary, ternary, and quaternary aluminosilicate glasses are also shown (alkali silicate glasses [black circle, $Na_2O$:$SiO_2$ = 1:2, ref. 57; blue square, $Na_2O$:$SiO_2$ = 1:3, ref. 37; red open circle, $Na_2O$:$SiO_2$ = 1:4, ref. 58], ternary mixed-cation silicates [black square, $Na_2O$:CaO:$SiO_2$ = 0.75:0.25:3, ref. 25], depolymerized aluminosilicate glasses [black triangle, $Na_2O$:$Al_2O_3$:$SiO_2$ = 1.5:0.5:6, ref. 37; open triangle, $Na_2O$:$Al_2O_3$:$SiO_2$ = 3:1:4, ref. 40; diamond, $[(Na_2O)_{0.75}(CaO)_{0.25}]$:$Al_2O_3$:$SiO_2$ = 3:1:4, ref. 26]).

Downloaded at California Institute of Technology on September 8, 2020

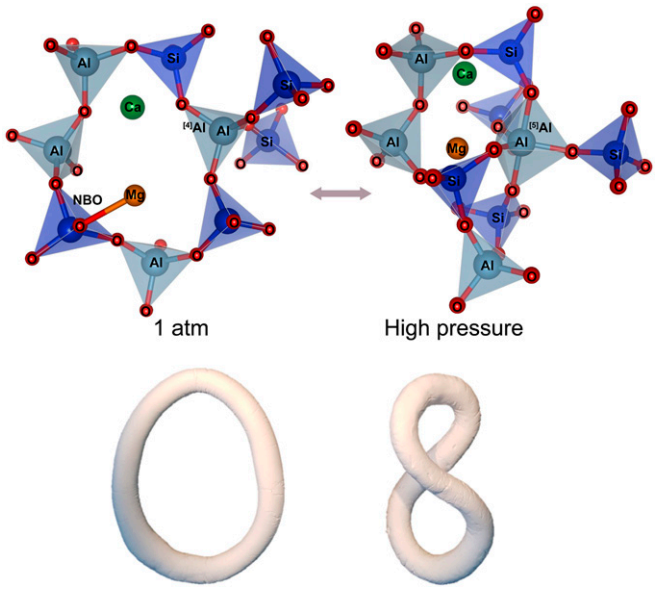


**Fig. 3.** Schematic structure and densification mechanism of model basaltic melts. (*Top*) Schematic structure of model basaltic melts at 1 atm and 5 GPa. One bond between Mg and NBO is shown to demonstrate the role of Mg as a network modifying cation at 1 atm (*SI Appendix*, section S6). (*Bottom*) Densification mechanism based on ring twist from O-ring topology to twisted ∞ topology in the melts under compression.

change in configuration entropy that is associated with the change in topology (stemming from the coordination transformation).

The number of configurations that a network adopts at particular pressure–temperature conditions is directly related to its configurational entropy ($S_{conf}$) via Boltzmann's entropy formula, and a convenient way to count the available configurations in a silicate network is through the populations of oxygen species. Hence, the ability to extract changes in the proportions of each type of BO and NBO translates into constraints on the pressure dependence of $S_{conf}$ (*SI Appendix*, sections S7 and S8). In aluminosilicate melts, one key order parameter that influences the population of BO among $^{[4,5,6]}$Al and $^{[4]}$Si is the degree of Al avoidance ($Q$) that is scaled to vary from 1 for a fully ordered Al-Si network with complete Al avoidance to 0 for a random Si-Al distribution (45). Based on data on Ca-aluminosilicate and Mg-aluminosilicate glasses (26, 45), the $Q$ value in the model basalt is 0.77, indicating a moderate preference for Si-Al ordering (*SI Appendix*, section S7). At 1 atm, where essentially all of the Al is $^{[4]}$Al (Fig. 1), $Q$ = 0.77 implies that the fractions of NBO, $^{[4]}$Si-O-$^{[4]}$Al, $^{[4]}$Si-O-$^{[4]}$Si, and $^{[4]}$Al-O-$^{[4]}$Al in the glass at 1 atm should be 38, 29, 26, and 7%, respectively (26, 45). At 5 GPa, as Si-O-$^{[5,6]}$Al forms at the expense of NBO and $^{[4]}$Si-O-$^{[4]}$Al and $Q$ values do not change significantly, the estimated fractions at 5 GPa of NBO, $^{[4]}$Si-O-$^{[4]}$Al, $^{[4]}$Si-O-$^{[4]}$Si, $^{[4]}$Al-O-$^{[4]}$Al, and $^{[4]}$Si-O-$^{[5,6]}$Al are then 32, 22, 26, 7, and 13%, respectively (26, 45, 46). The formation of $^{[5,6]}$Al creates a more diverse set of configurations over which the oxygen atoms of the network distribute themselves upon compression. This corresponds to an overall increase in $S_{conf}$ from ∼10.5 J/K per mole of O at 1 atm to ∼12.5 J/K per mole of O at 5 GPa (*SI Appendix*, section S8). $S_{conf}$ is expected to continue increasing with a further increase in pressure as the abundance of major oxygen species become subequal but would eventually decrease with increasing pressure above the threshold pressure where the maximum dispersion of configurations is reached (Fig. 4) (*SI Appendix*, sections S8 and S9).

Turning to the implications of these results for understanding the anomalous compression and viscosity of silicate melts (37, 47), we note that both properties can be seen to depend on the flexibility (or, conversely, the rigidity) of the network. $S_{conf}$ quantifies the degrees of configurational freedom in the melt network and hence its flexibility to accommodate compression through configurational changes. In contrast, decreases in molar volume increase network rigidity as denser packing places the atoms farther toward the repulsive portions of their mutual force interactions. As pressure increases, the molar volume of Columbia River basalt (BCR-2) and $Di_{64}An_{36}$ melts each decrease by 15% from 1 atm to 5 GPa (14) (Fig. 4, *Top*, and *SI Appendix*, section S10). The entropy effect (i.e., the increase in network flexibility) is dominant in the low-pressure range, while densification (i.e., the increase in network rigidity) prevails at higher pressure. These two competing effects therefore determine the overall flexibility of the network and are manifested as a nonlinear variation in elastic properties. This can be observed by plotting the inverses of the elastic wave velocities ($1/V_s$ and $1/V_p$) against pressure; the inverse wave speeds in BCR-2 and in Icelandic Basalt (BIR-1) all show maxima at pressures of ∼1.5 to 5 GPa (7, 13–15, 29, 32) (Fig. 4, *Top*). If such anomalous softening is explained by two competing mechanisms, one tied to the increase in $S_{conf}$ and one to the decrease in melt volume ($V$), then the net effect can be parameterized by pressure-induced changes in the product $\overline{S}_{conf}*V$ (here $\overline{S}_{conf}$ is normalized to $S_{conf}$ at 1 atm) (Fig. 4, *Top Right*, and *SI Appendix*, Fig. S4 and section S5). Because $S_{conf}$ also decreases at higher-pressure conditions beyond the threshold pressure described above, the rigidity of the melt network is expected to eventually increase, and the region of anomalous compression will end. The current link between the structures and elastic constants is not fully quantitative as the effect of temperature and composition on the aforementioned properties needs to be further constrained (*SI Appendix*, sections S8 and S11). The current model is therefore designed to provide a conceptual model of changes in melt properties as the result of changes in two competing variables, configurational entropy and density.

Given the intrinsic uncertainty in melt volume and structure under compression at high temperature, extensive effort remains before the nature of structural transformation in oxide melts at higher temperature and pressure is fully understood. Currently, the structural data above 5 GPa and the possible structural transitions involving $^{[5,6]}$Si are unknown, although it is clear that highly coordinated Si becomes prevalent above ∼15 GPa. The formation of these structures above 15 GPa may increase the configurational entropy. It is also expected that the configurational disorder of liquids at high temperature is larger than that in corresponding glasses. The effect of temperature is currently difficult to quantify, as detailed in situ study of Al speciation in multicomponent melts and the degree of mixing at high pressure remains to done. Earlier experimental and theoretical studies of simple oxide glasses and melts show that the average coordination environment between glasses and melts is not significantly different (*SI Appendix*, section S11). Qualitatively, the larger configurational entropy at higher temperature shifts the pressure conditions for the entropy maximum.

The topological geometric transformation model in the current study is more suitable to describing the pressure-induced structural transitions in glasses at low temperature but may not fully capture the compression of liquids at high temperature, which are also influenced by atomic dynamics. Nevertheless, we note that such topological changes are consistent with the observed changes in NMR spectra for the glasses quenched from the supercooled liquids: the topological contraction is one way to accommodate the formation of highly coordinated Al. Thus, the current model shows a possible topological transition in melts upon compression. Furthermore, in the current case of basaltic glasses and melts, the coordination transformation in Al and related topological changes are responsible for the pressure-induced



Downloaded at California Institute of Technology on September 8, 2020

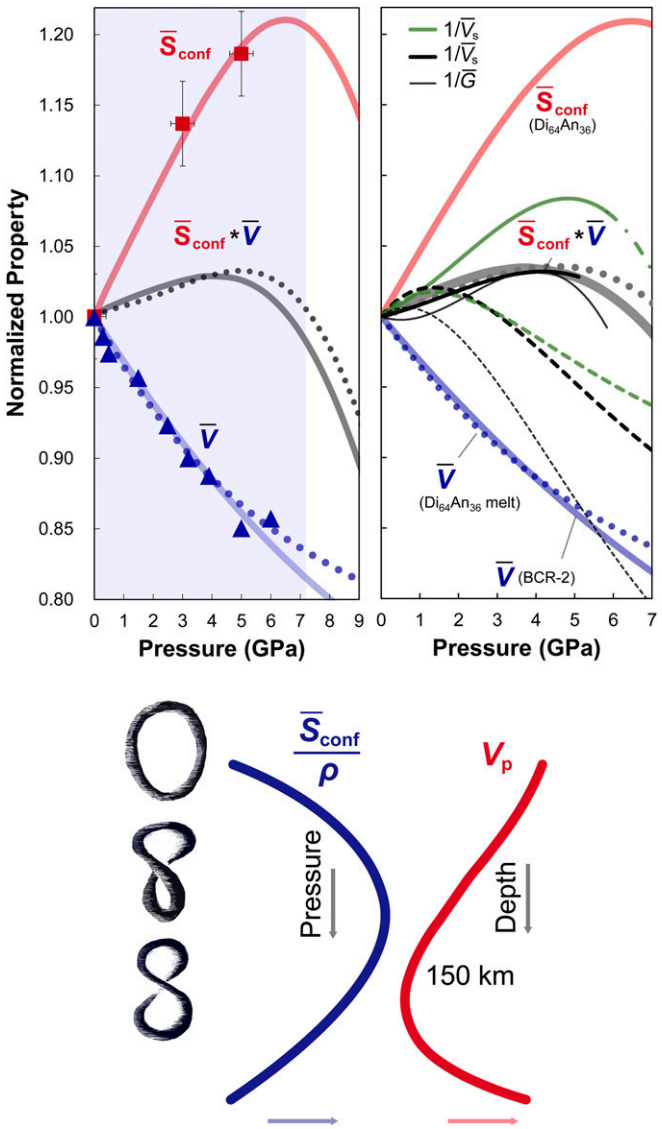


**Fig. 4.** Structure, configurational entropy, and anomalous compression of basaltic melts. (*Top Left*) Effect of pressure on the normalized configurational entropy ($\overline{S}_{conf}$, red square, $Di_{64}An_{36}$, in this study), volume ($\overline{V}$, blue dotted line, $Di_{64}An_{36}$ melts, ref. 32; blue solid line, BCR-2, ref. 14), and $\overline{S}_{conf}$*$\overline{V}$ (thick gray solid line, $\overline{S}_{conf}$ from $Di_{64}An_{36}$ glasses and $\overline{V}$ from BCR-2). $Di_{64}An_{36}$, BIR-1, and BCR-2 refer to glasses in diopside-anorthite eutectic composition, Icelandic basalt glasses, and Columbia River basalt glasses, respectively (*SI Appendix*, Table S3). Pale blue box depicts the range that is highlighted in *Top Right*. (*Top Right*) Effect of pressure on the normalized shear modulus ($1/\overline{G}$, thin black broken line, BIR-1, ref. 15; thin black solid line, BCR-2, ref. 14), P wave velocity ($1/\overline{V}_p$, thick black broken line, BIR-1, ref. 15; thick black broken line, BIR-1, ref. 15; thick black solid line, BCR-2, ref. 14), and S wave velocity ($1/\overline{V}_s$, green broken line, BIR-1, ref. 15; green solid line, BCR-2, ref. 14). The green dot plus a solid line refers to the extrapolation of $1/\overline{V}_s$ (BCR-2) above ~5 GPa. $V_s$ and the density of BCR-2 glass were studied up to only 5 GPa. Therefore, the data from 5 to 7 GPa are extrapolated from the data up to 5 GPa. These normalized elastic properties are compared with $\overline{S}_{conf}$*$\overline{V}$. (*Bottom*) Schematic figure describing the simplified structural evolution of basaltic melts based on ring topology (black) and its effect on $\overline{S}_{conf}/\rho$ (thick blue solid line) and $V_s$ (red solid line) of basaltic glasses with varying pressure. The gray, blue, and red arrows denote the directions of increasing depth, $\overline{S}_{conf}/\rho$, and $V_s$, respectively. *Bottom* combines the information from Fig. 3 and *Top* to assemble the topological model and its inferred consequences into a single framework.

changes in $S_{conf}$. In fully polymerized glasses such as $SiO_2$ glass, without any coordination transformation, only the topological transformation can lead to changes in $S_{conf}$. Therefore, the current model can be further generalized to cases where strictly topological contributions to $S_{conf}$ account for elastic properties of the compressed glasses.

Despite such complications, the observed structural changes in basaltic melts, becoming gradually more entangled due to formation of highly coordinated Al species and gaining additional entropy (scaled with density), provide clear atomistic insights into anomalous pressure-induced softening at depths down to ~150 km and pressures in the range of 2 to 5 GPa (Fig. 4, *Bottom*). While the contribution of such changes in the elasticity of the melt to the seismic properties of the bulk partially molten rock may be too small to be readily observed, the effects of $S_{conf}$ contribute to reaching a complete understanding of the need for melt, and the necessary quantity of such melt, to explain the softening near the LAB and deep below MOR. In an analogous way, because shear deformation requires that a melt network rearrange to an adjacent configuration and also that atoms be able to pass between one another, viscosity decreases with increasing $S_{conf}$ (48, 49) and increases with decreasing molar volume. The minimum in viscosity inferred from maxima in diffusivity of network-forming elements in silicate melts at moderate pressure (50–52) can therefore be understood from the framework of the competing effects of increasing $S_{conf}$ and decreasing $V$ with initial compression (*SI Appendix*, section S12).

The observed structural evolution may also have implications for trace element affinity for silicate melts and hence for partitioning during melting and the chemical evolution of the Earth's mantle. As shown in Fig. 3, pressure-induced formation of highly coordinated Al is accompanied by a decrease in ring size, which results in the reduction of free space available for large ionic radius incompatible elements in the melt. A salient example is the important element pair uranium (U) and lead (Pb). Because radioactive U is the parent of stable Pb, their relative partitioning during melting determines the differential Pb-isotope ratio evolution of igneous rocks derived from partial melts and their residues in the mantle. U is reported to be a network modifier with affinity to NBO (53). Therefore, the decrease in NBO fraction upon compression suggests that incorporating U in magmas becomes more difficult. By contrast, Pb has higher covalence with nearby oxygen and can thus also act as a network former with BOs, such as Pb-O-Si (54). Therefore, Pb may be more easily incorporated in the melt at high pressure. Taken together, these effects may cause the relative order of U and Pb compatibility to change with pressure (*SI Appendix*, section S13).

Because of the importance of basaltic melts in the upper mantle, it is important to gain appreciation of their structures and properties at the pressure conditions where they are actually found in the Earth. Inferences about melting at depth must consider structures of melts that differ from those measured at ambient pressure. While the nature of silicate melts at 1 atm, which is directly relevant to their behavior during shallow crustal processes and eruption, is relatively well studied, the challenges of carrying out similar studies at elevated pressure remain. In this work we have relied on glasses quenched from high pressure to capture the structural changes in high-pressure melts at their glass transition temperature (*SI Appendix*, sections S11 and S14). The resulting insights into $S_{conf}$ of melts lead to predictions for the pressure evolution of those properties of melts that can be measured in situ at high pressure and temperature, which will ultimately provide tests of the utility of this theory.

## Materials and Methods

The $^{17}O$ enriched Ca–Mg aluminosilicate glasses ($CaO:MgO:Al_2O_3:SiO_2$ = 25:16:9:50 mol %) of eutectic composition in the anorthite ($CaAl_2Si_2O_8$)-diopside ($CaMgSi_2O_6$) join were synthesized from $CaCO_3$ and oxides (MgO,



Downloaded at California Institute of Technology on September 8, 2020

$Al_2O_3$, and $^{17}O$-enriched $SiO_2$). The $Si^{17}O_2$ was synthesized from the hydrolysis of $SiCl_4$ with 40% $^{17}O$ $H_2O$. Approximately 0.2 wt % of $Co_3O_4$ was added to reduce NMR collection time. The mixture was decarbonated and heated at 1,673 K and then quenched (55). The resulting CMAS glass was loaded into Pt capsules and run in a piston cylinder (for the synthesis at 3 GPa) or multianvil press with a 25/15 (octahedron edge length/truncated edge length of the anvils) assembly (for the synthesis at 5 GPa) at California Institute of Technology (36). The glasses were held above their liquidus temperature, at 1,873 K for 20 min at 3 GPa and 2,100 K for ∼10 min at 5 GPa, and then quenched by shutting off power to the heating elements. Considering the rapid initial quench rates (∼300 K/s), the structures of model basaltic glasses quenched from melts at high pressure represent those of supercooled liquids under compression at ∼3 and 5 GPa at the glass transition temperature. During quenching, the pressure conditions in the assembly may decrease somewhat from the target pressure of the run before reaching the glass transition (38, 56) (*SI Appendix*, section S15, for the detailed discussion). Three multicomponent basaltic glasses representing liquid compositions derived by low-degree partial melting of model (Fe-free) KLB-1 peridotite at 1 atm, 1.5 GPa, and 3 GPa were also synthesized at 1 atm by melting mixtures of oxides and carbonates. The fractions of MgO among the network-modifying cations in these synthetic glasses, $X_{MgO}$ = MgO/(CaO + MgO + $Na_2O$ + $K_2O$) are 0.46, 0.56, and 0.65 (*SI Appendix*, section S3 and Table S2). Note that it is challenging to synthesize Mg-rich aluminosilicate glasses at high pressure due to the higher melting temperature at high pressure and the formation of quench crystals (*SI Appendix*, section S15). Therefore, the experimental results for the model basaltic glass at high pressure provide a benchmark on what we can do more with the Mg-rich silicate melts (e.g., partial melts of KLB-1). The presence of volatiles ($H_2O$ and $CO_2$) on the structures and properties of melts cannot be fully addressed here as these have not been added in the glasses (*SI Appendix*, section S14).

The $^{27}Al$, $^{17}O$, and $^{29}Si$ NMR spectra were collected on a Varian 400 solid-state NMR spectrometer operating at 9.4 Tesla at Seoul National University. We used a 3.2-mm $ZrO_2$ rotor in a Varian double-resonance MAS probe. The $^{27}Al$ MAS and triple quantum (3Q) MAS NMR spectra for the model basaltic were collected at a Larmor frequency of 104.3 MHz using shifted-echo pulse sequences (3 μs–τ [delay]–1.1 μs–echo delay [∼0.5 ms]–15 μs). The spinning speed was 17 kHz with a recycle delay of 1 s with an external reference of 0.3 M $AlCl_3$ solution. The $^{17}O$ 3QMAS NMR were collected at a Larmor frequency of 54.23 MHz using a similar pulse sequence (3.3 μs–τ [delay]–0.7 μs–echo delay [∼0.5 ms]–15 μs) with a relaxation delay of 1 s and a magic-angle sample spinning speed of 15 kHz. The $^{17}O$ MAS NMR spectra for the glasses were collected using an *rf* pulse length of 0.3 μs. All spectra were referenced to tap water. The $^{29}Si$ MAS NMR spectra for the basaltic glasses were collected at a Larmor frequency of 79.4 MHz with a single 30° pulse of 0.6 μs and referenced to Tetramethylsilane solution. A delay of 30 s between pulses and a spinning speed of 11 kHz were used.

**Data Availability.** All study data are included in the article and *SI Appendix*.

**ACKNOWLEDGMENTS.** This study was supported by a grant from the National Research Foundation, Korea (2017R1A2A1A17069511 and 2020R1A3B2079815), to S.K.L. We appreciate reviewers' constructive comments, which greatly improved the quality and clarity of the manuscript.



1. A. W. Hofmann, Mantle geochemistry: The message from oceanic volcanism. *Nature* **385**, 219–229 (1997).
2. K. H. Rubin, J. M. Sinton, J. Maclennan, E. Hellebrand, Magmatic filtering of mantle compositions at mid-ocean-ridge volcanoes. *Nat. Geosci.* **2**, 321–328 (2009).
3. V. D. Wanless, A. M. Shaw, Lower crustal crystallization and melt evolution at mid-ocean ridges. *Nat. Geosci.* **5**, 651–655 (2012).
4. P. D. Asimow, C. H. Langmuir, The importance of water to oceanic mantle melting regimes. *Nature* **421**, 815–820 (2003).
5. Z. C. Eilon, G. A. Abers, High seismic attenuation at a mid-ocean ridge reveals the distribution of deep melt. *Sci. Adv.* **3**, e1602829 (2017).
6. R. Dasgupta *et al*., Carbon-dioxide-rich silicate melt in the Earth's upper mantle. *Nature* **493**, 211–215 (2013).
7. D. Andrault *et al*., Toward a coherent model for the melting behavior of the deep Earth's mantle. *Phys. Earth Planet. Inter.* **265**, 67–81 (2017).
8. D. H. Green, W. O. Hibberson, I. Kovács, A. Rosenthal, Water and its influence on the lithosphere-asthenosphere boundary. *Nature* **467**, 448–451 (2010).
9. A. Pommier *et al*., Experimental constraints on the electrical anisotropy of the lithosphere-asthenosphere system. *Nature* **522**, 202–206 (2015).
10. T. Sakamaki *et al*., Ponded melt at the boundary between the lithosphere and asthenosphere. *Nat. Geosci.* **6**, 1041–1044 (2013).
11. T. A. Stern *et al*., A seismic reflection image for the base of a tectonic plate. *Nature* **518**, 85–88 (2015).
12. D. B. Dingwell, "Properties of rocks and minerals-diffusion, viscosity, and flow of melts" in *Treatise on Geophysics*, G. Schubert, Ed. (Elsevier, Amsterdam, 2007), Vol. vol. 2, pp. 419–436.
13. A. N. Clark, C. E. Lesher, Elastic properties of silicate melts: Implications for low velocity zones at the lithosphere-asthenosphere boundary. *Sci. Adv.* **3**, e1701312 (2017).
14. A. N. Clark, C. E. Lesher, S. D. Jacobsen, Y. Wang, Anomalous density and elastic properties of basalt at high pressure: Reevaluating of the effect of melt fraction on seismic velocity in the Earth's crust and upper mantle. *J. Geophys. Res.* **121**, 4232–4248 (2016).
15. J. Liu, J. F. Lin, Abnormal acoustic wave velocities in basaltic and (Fe, Al)-bearing silicate glasses at high pressures. *Geophys. Res. Lett.* **41**, 8832–8839 (2014).
16. B. O. Mysen, P. Richet, *Silicate Glasses and Melts: Properties and Structure*, (Developments in Geochemistry, Elsevier, Amsterdam, 2005), p. 560.
17. J. F. Stebbins, Glass structure, melt structure, and dynamics: Some concepts for petrology. *Am. Mineral.* **101**, 753–768 (2016).
18. D. Andrault *et al*., Solidus and liquidus profiles of chondritic mantle: Implication for melting of the Earth across its history. *Earth Planet. Sci. Lett.* **304**, 251–259 (2011).
19. M. Bouhifd, A. Jephcoat, Convergence of Ni and Co metal–silicate partition coefficients in the deep magma-ocean and coupled silicon–oxygen solubility in iron melts at high pressures. *Earth Planet. Sci. Lett.* **307**, 341–348 (2011).
20. G. A. Gaetani, The influence of melt structure on trace element partitioning near the peridotite solidus. *Contrib. Mineral. Petrol.* **147**, 511–527 (2004).
21. S. C. Kohn, P. F. Schofield, The importance of melt composition in controlling trace-element behavior—An experimental-study of Mn and Zn partitioning between forsterite and silicate melts. *Chem. Geol.* **117**, 73–87 (1994).
22. B. O. Mysen, Element partitioning between minerals and melt, melt composition, and melt structure. *Chem. Geol.* **213**, 1–16 (2004).
23. M. Roskosz, M. A. Bouhifd, A. Jephcoat, B. Marty, B. Mysen, Nitrogen solubility in molten metal and silicate at high pressure and temperature. *Geochim. Cosmochim. Acta* **121**, 15–28 (2013).
24. B. J. Wood, J. D. Blundy, "Trace element partitioning: The influences of ionic radius, cation charge, pressure, and temperature" in *Treatise on Geochemistry*, H. D. Holland, K. K. Turekian, Eds. (Elsevier, Oxford, ed. 2, 2014), Vol. vol. 3, pp. 421–448.
25. S. K. Lee, G. D. Cody, Y. Fei, B. O. Mysen, Oxygen-17 nuclear magnetic resonance study of the structure of mixed cation calcium-sodium silicate glasses at high pressure: Implications for molecular link to element partitioning between silicate liquids and crystals. *J. Phys. Chem. B* **112**, 11756–11761 (2008).
26. S. K. Lee, Simplicity in melt densification in multicomponent magmatic reservoris in Earth's interior revealed by multinuclear magnetic resonance. *Proc. Natl. Acad. Sci. U.S.A.* **108**, 6847–6852 (2011).
27. S. K. Lee *et al*., Quasi-equilibrium melting of quartzite upon extreme friction. *Nat. Geosci.* **10**, 436–441 (2017).
28. J. A. C. Robinson, B. J. Wood, The depth of the spinel to garnet transition at the peridotite solidus. *Earth Planet. Sci. Lett.* **164**, 277–284 (1998).
29. D. Tinker, C. E. Lesher, I. D. Hutcheon, Self-diffusion of Si and O in diopside-anorthite melt at high pressures. *Geochim. Cosmochim. Acta* **67**, 133–142 (2003).
30. K. Hirose, I. Kushiro, Partial melting of dry peridotites at high pressures: Determination of compositions of melts segregated from peridotite using aggregates of diamond. *Earth Planet. Sci. Lett.* **114**, 477–489 (1993).
31. S. Y. Park, S. K. Lee, Probing the structure of Fe-free model basaltic glasses: A view from a solid-state $^{27}Al$ and $^{17}O$ NMR study of Na-Mg silicate glasses, $Na_2O$-MgO-$Al_2O_3$-$SiO_2$ glasses, and synthetic Fe-free KLB-1 basaltic glasses. *Geochim. Cosmochim. Acta* **238**, 563–579 (2018).
32. Y. Ai, R. A. Lange, New acoustic velocity measurements on CaO-MgO-$Al_2O_3$-$SiO_2$ liquids: Reevaluation of the volume and compressibility of $CaMgSi_2O_6$-$CaAl_2Si_2O_8$ liquids to 25 GPa. *J. Geophys. Res.* **113**, B04203 (2008).
33. T. Sakamaki *et al*., Contrasting sound velocity and intermediate-range structural order between polymerized and depolymerized silicate glasses under pressure. *Earth Planet. Sci. Lett.* **391**, 288–295 (2014).
34. Y. Wang *et al*., Atomistic insight into viscosity and density of silicate melts under pressure. *Nat. Commun.* **5**, 3241 (2014).
35. J. R. Allwardt *et al*., Aluminum coordination and the densification of high-pressure aluminosilicate glasses. *Am. Mineral.* **90**, 1218–1222 (2005).
36. K. E. Kelsey *et al*., Cation field strength effects on high pressure aluminosilicate glass structure: Multinuclear NMR and La XAFS results. *Geochim. Cosmochim. Acta* **73**, 3914–3933 (2009).
37. S. K. Lee, G. D. Cody, Y. W. Fei, B. O. Mysen, Nature of polymerization and properties of silicate melts and glasses at high pressure. *Geochim. Cosmochim. Acta* **68**, 4189–4200 (2004).
38. S. Bista, J. F. Stebbins, W. B. Hankins, T. W. Sisson, Aluminosilicate melts and glasses at 1 to 3 GPa: Temperature and pressure effects on recovered structural and density changes. *Am. Mineral.* **100**, 2298–2307 (2015).
39. J. L. Yarger *et al*., Al coordination changes in high-pressure aluminosilicate liquids. *Science* **270**, 1964–1967 (1995).
40. S. K. Lee *et al*., Effect of network polymerization on the pressure-induced structural changes in sodium aluminosilicate glasses and melts: $^{27}Al$ and $^{17}O$ solid-state NMR study. *J. Phys. Chem. C* **116**, 2183–2191 (2012).
41. T. Irifune, T. Tsuchiya, "Phase transitions and mineralogy of the lower mantle" in *Treatise on Geophysics*, G. Schubert, Ed. (Elsevier, Oxford, ed. 2, 2015), Vol. vol. 2, pp. 33–60.

Downloaded at California Institute of Technology on September 8, 2020

42. A. Zeidler *et al*., High-pressure transformation of $SiO_2$ glass from a tetrahedral to an octahedral network: A joint approach using neutron diffraction and molecular dynamics. *Phys. Rev. Lett.* **113**, 135501 (2014).
43. B. T. Poe *et al*., Silicon and oxygen self-diffusivities in silicate liquids measured to 15 gigapascals and 2800 Kelvin. *Science* **276**, 1245–1248 (1997).
44. E. M. Stolper, T. J. Ahrens, On the nature of pressure-induced coordination changes in silicate melts and glasses. *Geophys. Res. Lett.* **14**, 1231–1233 (1987).
45. S. K. Lee, H.-I. Kim, E. J. Kim, K. Y. Mun, S. Ryu, Extent of disorder in magnesium aluminosilicate glasses: Insights from $^{27}$Al and $^{17}$O NMR. *J. Phys. Chem. C* **120**, 737–749 (2016).
46. S. K. Lee, J. F. Stebbins, Extent of intermixing among framework units in silicate glasses and melts. *Geochim. Cosmochim. Acta* **66**, 303–309 (2002).
47. Y. Bottinga, P. Richet, Silicate melts: The "anomalous" pressure dependence of the viscosity. *Geochim. Cosmochim. Acta* **59**, 2725–2731 (1995).
48. G. Adam, J. H. Gibbs, On the temperature dependence of cooperative relaxation properties in glass-forming liquids. *J. Chem. Phys.* **43**, 139–146 (1965).
49. P. Richet, Viscosity and configurational entropy of silicate melts. *Geochim. Cosmochim. Acta* **48**, 471–483 (1984).
50. E. S. Persikov, P. G. Bukhtiyarov, A. G. Sokol, Viscosity of haplokimberlitic and basaltic melts at high pressures: Experimental and theoretical studies. *Chem. Geol.* **497**, 54–63 (2018).
51. E. S. Posner, B. Schmickler, D. C. Rubie, Self-diffusion and chemical diffusion in peridotite melt at high pressure and implications for magma ocean viscosities. *Chem. Geol.* **502**, 66–75 (2018).
52. J. E. Reid *et al*., The viscosity of $CaMgSi_2O_6$ liquid at pressures up to 13 GPa. *Phys. Earth Planet. Inter.* **139**, 45–54 (2003).
53. F. Farges, C. W. Ponader, G. E. Brown, Structural environments of incompatible elements in silicate glass melt systems. 1. Zirconium at trace levels. *Geochim. Cosmochim. Acta* **55**, 1563–1574 (1991).
54. S. K. Lee, E. J. Kim, Probing metal-bridging oxygen and configurational disorder in amorphous lead silicates: Insights from O-17 solid-state nuclear magnetic resonance. *J. Phys. Chem. C* **119**, 748–756 (2015).
55. S. Y. Park, S. K. Lee, Structure and disorder in basaltic glasses and melts: Insights from high-resolution solid-state NMR study of glasses in diopside–Ca-tschermakite join and diopside–anorthite eutectic composition. *Geochim. Cosmochim. Acta* **80**, 125–142 (2012).
56. S. J. Gaudio, C. E. Lesher, H. Maekawa, S. Sen, Linking high-pressure structure and density of albite liquid near the glass transition. *Geochim. Cosmochim. Acta* **157**, 28–38 (2015).
57. X. Xue, J. F. Stebbins, M. Kanzaki, Correlations between O-17 NMR parameters and local structure around oxygen in high-pressure silicates and the structure of silicate melts at high pressure. *Am. Mineral.* **79**, 31–42 (1994).
58. S. K. Lee, G. D. Cody, Y. W. Fei, B. O. Mysen, The effect of Na/Si on the structure of sodium silicate and aluminosilicate glasses quenched from melts at high pressure: A multi-nuclear (Al-27, Na-23, O-17) 1D and 2D solid-state NMR study. *Chem. Geol.* **229**, 162–172 (2006).

Downloaded at California Institute of Technology on September 8, 2020